Investigation into the Hot-Forming Limit for 22MnB5 Hot-Forming Steel under a Stamping Process

Wenwu He [1], Bin Yang [1], Xuezhong Zhang [1], Min Li [2], Shuli Sun [1], Bao Wang [1,*] and Qingxian Ma [3]

1   School of Materials Science & Engineering, Taiyuan University of Science and Technology, Taiyuan 030024, China
2   Weichai Power Co., Ltd., Weifang 261061, China
3   Department of Mechanical Engineering, Tsinghua University, Beijing 100084, China
*   Correspondence: baowang@tyust.edu.cn; Tel.: +86-035-1216-1126

Abstract: Hot-forming technology for 22MnB5 hot-forming steel (22MnB5 HF steel) plates has been widely used in the automobile manufacturing industry in recent years. Physical simulation and numerical modeling were carried out in order to determine the forming limit of a 22MnB5 steel plate for the stamping process. The deformation experiments were performed in a temperature range of 600~900 °C and a strain rate range of 0.1~10 s^{-1}. In the uniaxial tensile tests, it was found that at the forming temperature of 600 °C, the condition of dynamic recrystallization was not fully reached, and thus the corresponding tensile strength was much larger than that at other deformation temperatures. In the numerical simulation of bulging experiments, it was found that 22MnB5 steel had good formability when the initial deformation temperature was high and the forming speed was low by using the instability criterion, combining the maximum punch force and strain path transition. The forming limit diagram of 22MnB5 steel at a temperature of 700 °C and tool speed of 25 mm/s was obtained by means of simulation and a hot stamping experiment. The establishment of the forming limit of the 22MnB5 steel plate can provide theoretical and technical guidance for the hot-forming process.

Keywords: 22MnB5 hot-forming steel; forming limit diagram; fracture criterion; numerical simulation

1. Introduction

With the development of social economy and the improvement in per capita income, the automobile manufacturing industry has developed rapidly. At the same time, the automobile manufacturing industry has also put forward higher requirements for material resources and environmental protection [1–3]. The body steel plate accounts for more than 20% of the total weight of the vehicle. Experiments have shown that if the vehicle mass is reduced by 100 kg, the fuel consumption for driving 100 km can be reduced by 0.3–0.6 L. Fuel consumption can be reduced by 0.7% for every 1% reduction in vehicle weight [4,5]. According to statistics, at present, 90% of the steel plates used in automobiles are made of HF steel. The use of HF steel plates as automobile body manufacturing materials has reduced the total mass of automobiles by about 30% compared with the use of ordinary steel plates. This 22MnB5 steel has the advantages of high strength and excellent collision resistance. The use of HF steel plates can meet the performance requirements and achieve lightweight automobiles [6–8]. Therefore, it has become the preferred material for automobile structural parts of many automobile enterprises [9].

However, the excellent strength also causes many problems and defects in the stamping process of HF steel at room temperature [10,11]. The hot stamping technology of HF steel can avoid the disadvantages of easy wrinkling and cracking of materials at room temperature, the poor forming quality of workpieces, high requirements for equipment and the easy damage of molds [12–14]. Therefore, the hot-forming technology of the HF steel plate has become a hot research topic [15,16]. Germany and Sweden have an absolute

leading position and voice in the R&D field of hot stamping. Melak et al. studied the influence of plate thickness and cooling medium on the hot stamping quality of the 22MnB5 steel plate by combining experimental and simulation methods. It was found that increasing the plate thickness and changing the cooling medium can improve the strength and toughness of the parts [17]. Daniel et al. studied the transformation temperature and critical cooling rate of the 22MnB5 steel plate with Zn–Fe coating during hot forming by means of microscopic characterization [18]. Venturato et al. established the generalized incremental stress-state-dependent damage model (GISSMO) to predict the formability in 22MnB5 hot stamping by means of experiment and numerical simulation [19]. Zhuang et al. conducted X-ray diffraction and microstructure investigations to study the phase composition and micro defects, respectively, established a damage-coupled pre-forming constitutive model, and embedded it into ABAQUS 2016 through the VUMAT interface for simulation [20]. Chen et al. proposed a theoretical prediction model for forming a limit prediction model for the high temperature forming process of 22MnB5 based on the Norton–Hoff constitutive model, BBC 2005 yield criterion, and M-K model [21]. Zhou et al. used the combination of theoretical research, finite element simulation, and an experimental test to realize the three-field coupling of thermal mechanical damage in the hot stamping process by using the numerical simulation method [22]. Guo and Zhang et al. introduced the Zener Hollomon parameter to improve the Cockcroft–Latham criterion, Rice–Tracey criterion, and Oyane criterion to predict the initial value of damage and fracture of relevant materials [23,24]. But for the 22MnB5 steel sheet, there is a lack of forming limit research combining simulation and hot stamping experiments. The plasticity of the material in the high-temperature forming process will be affected by the temperature and deformation speed. The steel plate and the heat exchange with the mold will also affect the final experimental results, so it is difficult to obtain a more accurate thermal forming limit.

In the present study, through hot tensile tests and the numerical simulation of bulging tests on 22MnB5 steel, the microstructural changes of 22MnB5 steel and the thermoplasticity of the material under different deformation conditions were analyzed. The fracture criterion and hot-forming limit diagram were established to predict the fracture failure behavior of 22MnB5 steel.

2. Materials and Methods

2.1. Numerical Simulation of Stamping Forming

The material used in the present study was a 22MnB5 steel plate with a thickness of 1.4 mm, and the chemical composition is summarized in Table 1.

Table 1. Chemical composition of the studied 22MnB5 steel (Mass fraction, at. %).

Element	C	Mn	P	S	Si	Ti + Cr	B	Fe
Content (at. %)	0.22	1.2	0.019	0.003	0.25	0.229	0.003	Bal.

The hot tensile test of 22MnB5 steel was carried out on the Gleeble1500D thermal simulation test machine (Poestenkill, NY, USA). The tensile sample width was 14.5 mm and the length was 60 mm. After the sample was broken, the part near the fracture section was taken for metallographic observation. The sample was polished with 240–1000 mesh sandpaper and then mechanically polished to obtain the metallographic sample. The geometric model of the bulging experiment was established as shown in Figure 1. The plate thickness of 22MnB5 steel was set to 1.4 mm and the length to 180 mm. To change the strain path of the 22MnB5 steel plate, 9 different plate widths were set at 20 mm intervals between 20 mm and 180 mm, and the punch diameter was set to 100 mm. The material model required by 22MnB5 steel plate and die was obtained, and DYNAFORM 5.9.4 finite element simulation software was used to simulate the bulging test of the 22MnB5 steel plate. The initial temperature of the 22MnB5 steel and the stamping deformation speed were changed, appropriate instability criteria were selected, and the influence of deformation

conditions on the formed parts was analyzed. The no. 106 material model was selected for this simulation. The model requires input material density, elastic modulus, Poisson's ratio, viscosity parameters C and P, thermal expansion coefficient, and stress–strain data, and the material parameters required for 22MnB5 steel by performing a tensile test and using JMatPro V7.0 simulation software. The voce hardening law saturation stress hardening model was used to perform the flow stress curves, corresponding to different temperatures of the 22MnB5 steel line fitting. The hot material parameters of 22MnB5 steel and H13 hot-work die steel were obtained using JMatPro simulation software.
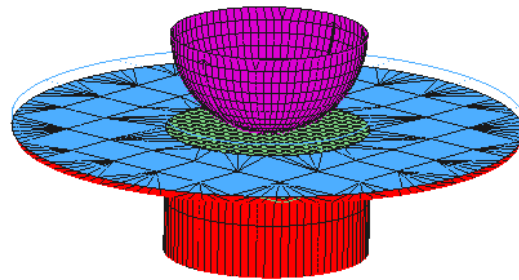
Figure 1. Geometric model of experimental die for Nakazima bulging.

2.2. Selection of Instability Criteria

The 22MnB5 steel is greatly affected by the value of the strain rate sensitivity index in the hot-forming process, and the error of forming limit diagram (FLD) function directly provided by the software was very large. Therefore, the instability criterion was needed to determine whether necking fracture occurred and to find out the fracture time. At present, the maximum punch force criterion and the strain path transition criterion are commonly used in the post-processing analysis of 22MnB5 steel numerical simulation.

Figure 2 shows the punch force–time curve corresponding to the samples taken from 22MnB5 steel plates with widths of 20 mm (Figure 2a), 80 mm (Figure 2b), 100 mm (Figure 2c), and 180 mm (Figure 2d). Through the cup bulging simulation of 22MnB5 steel with different plate widths, it was found that the maximum punch force criterion was only applicable to the small 22MnB5 steel width (20~80 mm). When the 22MnB5 steel width was relatively large (100~180 mm), the specimen would show a double tension state, and the punch force would increase with the growth of displacement without peak value.
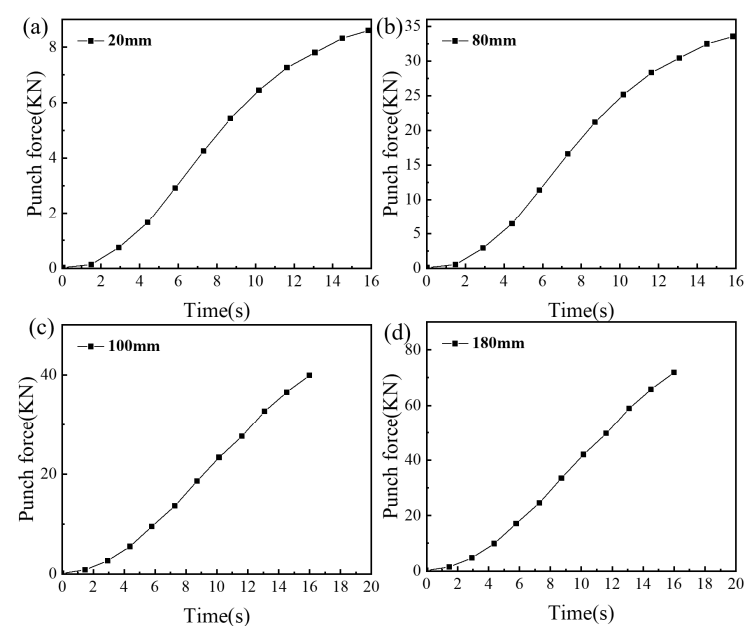
Figure 2. Punch force–time curve corresponding to samples with different widths: (**a**) 20 mm; (**b**) 80 mm; (**c**) 100 mm; (**d**) 180 mm.

Figure 3 presents the transition diagram of the maximum principal strain path corresponding to the specimen when the plate widths are 20 mm and 180 mm. It can be observed that when the plate width is small (less than 100 mm), there will be no inflection point in the strain path of the maximum principal strain, as shown in Figure 3a. When the second principal strain value is almost unchanged, but the maximum principal strain value increases sharply in a vertical shape, the stress state changes to a plane stress state, and the strain corresponding to the inflection point is the limit strain value, as shown in Figure 3b.
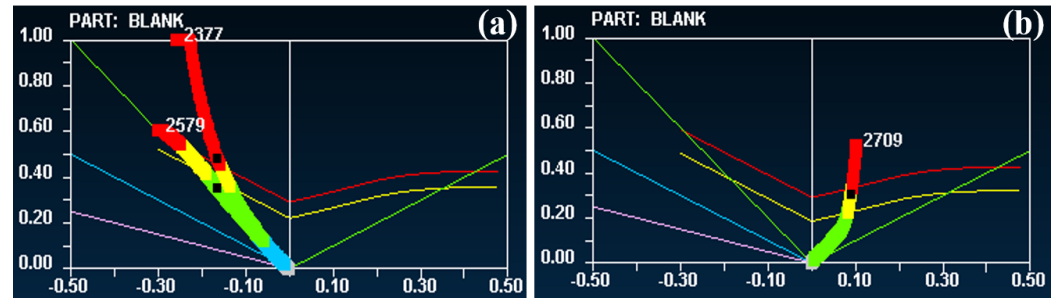
Figure 3. Transition diagram of maximum principal strain path corresponding to samples with different widths: (**a**) 20 mm; (**b**) 180 mm.

2.3. Hot-Stamping-Forming Experiment

On a THP-500T isothermal forging press (Genertec Tianduan, Tianjin, China), an experimental platform for hot stamping was independently set up, including a set of hot stamping dies according to the Nakazima bulging test standard, as well as displacement and force-measurement systems, as shown in Figure 4. The material of the hot stamping die was H13 steel. The hot stamping process parameters referred to the numerical simulation analysis results. Combined with the time–temperature transformation (TTT) curve of 22MnB5 provided by scholars [25], the steel that achieves austenitizing above 900 °C has better formability. The mold was first heated to 650 °C, and then the plate was heated to 930 °C by the resistance furnace, and the heat was maintained for 5 to 10 min. When the plate temperature was 700 °C, the plate was quickly transferred to the mold, and the experiment was carried out on the THP-500T isothermal forging press.

Figure 4. Hot-stamping-forming experiment equipment.

3. Results and Discussion

3.1. Mechanical Performance of the Studied 22MnB5 Steel Plate

The material was heated at a constant rate of 15 °C/s, the heated to 930 °C for 2 min, and the material was completely austenitized. Then, it was cooled to 600 °C~900 °C for the tensile test. The tensile stress–strain curves of 22MnB5 steel under different experimental conditions are presented in Figure 5. The tensile strength of 22MnB5 increased with the decrease in deformation temperature and rise in strain rate. The phenomenon of the strength obtained at temperature of 600 °C being the largest compared to the strength obtained at the other temperatures could be understood through the thermodynamic equilibrium transformation law of the studied steel, as is shown in Figure 6. Figure 6a shows the equilibrium transition diagram of the studied steel calculated through J-mat Pro software, and it could be seen that the A3, A1 temperatures were similarly determined to be 818 °C and 697 °C, and it could be further seen that the tensile temperature zones were mainly distributed in the dual-phase region consisting of ferrite and austenite. Figure 6b shows the continuous cooling transformation curves (CCT) of the studied steel calculated through J-mat Pro software. In accordance with the CCT, it could be seen that the undercooling austenite of the studied steel began to transform to pearlite when the tensile temperature decreased to 600 °C and 1 °C/s was selected as the cooling rate, and the microstructure was mainly composed of proeutectoid ferrite and pearlite. When the tensile temperature was increased to a certain temperature above ~650 °C, the microstructure of the studied steel was composed of proeutectoid ferrite and austenite in terms of the CCT, and it could be further deduced that the strength obtained at the tensile temperature of 600 °C was higher compared to the strength obtained at a tensile temperature above 650 °C due to the presence of the hardened phase of pearlite. According to the flow stress curve of 22MnB5 steel (Figure 5), the tensile strength and fracture strain of different tensile temperatures and strain rates could be obtained, as shown in Table 2. The fracture strain of the material increased with the increase in deformation temperature, and the fracture strain increased first and then decreased with the increase in strain rate (0.1–10 s^{-1}). Therefore, it can be preliminarily judged that the hot-stamping-forming interval of the 22MnB5 steel plate can be selected to be between 700 and 900 °C.
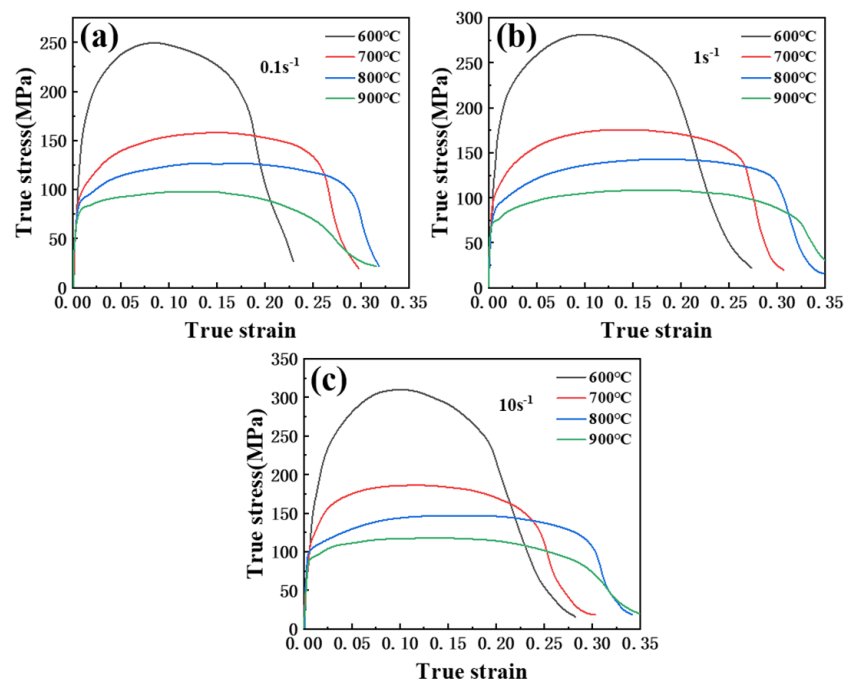
Figure 5. The 22MnB5 steel stress–strain curves under different experimental conditions: (**a**) strain rate = 0.1 s^{-1}; (**b**) strain rate = 1 s^{-1}; (**c**) strain rate = 10 s^{-1}.
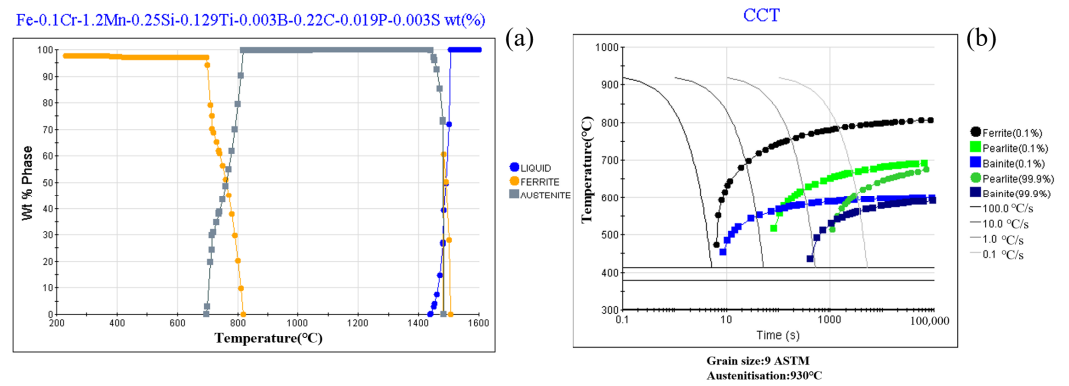
Figure 6. Equilibrium transition diagram and CCT of 22MnB5 steel. (**a**) The equilibrium transition diagram; (**b**) CCT curve.

Table 2. Tensile strength and fracture strain of 22MnB5 steel under different experimental conditions.

Temperature (°C)	600			700			800			900		
Strain rate (s^{-1})	0.1	1	10	0.1	1	10	0.1	1	10	0.1	1	10
Tensile strength (MPa)	250	284	310	158	177	192	127	143	148	98	109	121
Fracture strain	0.228	0.243	0.232	0.271	0.283	0.256	0.299	0.316	0.301	0.301	0.313	0.311

3.2. Influence of Deformation Conditions on Simulation Results under Stamping Experiment

For 180 × 180 mm 22MnB5 steel, the initial deformation temperature of 22MnB5 steel was set as 600 °C, 700 °C, 800 °C, or 900 °C, and the forming speed was 2.5 mm/s, 25 mm/s or 250 mm/s, respectively. The maximum principal strain unit was found, and the number of steps corresponding to the critical rupture time of the maximum principal strain unit was found using the strain path transformation criterion. The different deformations at critical rupture time were compared and analyzed under the conditions of 22MnB5 steel temperature field, pressure displacement, and thinning rate.

Figure 7 is the cloud chart of the equivalent plastic strain rate corresponding to different forming speeds. It can be found that when the forming speed is 2.5 mm/s, the equivalent plastic strain rate is particularly small, with a maximum of 0.062 s^{-1}. Although the strain rate nephogram is unevenly distributed, the small value does not affect the uniformity of the deformation area. With the increase in forming speed, the equivalent plastic strain rate increases continuously, and the difference in equivalent plastic strain rate corresponding to different deformation regions becomes larger, resulting in uneven deformation; fracture occurs more easily in the region with large equivalent strain rate.
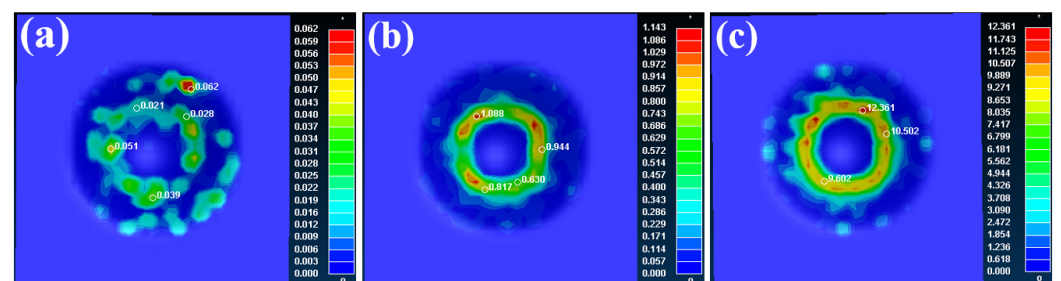
Figure 7. Nephogram of equivalent plastic strain rates under different forming speeds: (**a**) 2.5 mm/s; (**b**) 25 mm/s; (**c**) 250 mm/s.

Figure 8 is the nephogram of the plate-pressing displacement corresponding to the critical fracture time at different forming speeds. The maximum downforce displacements corresponding to the critical fracture time at different forming speeds were 27.308 mm,

23.506 mm, and 21.903 mm, respectively. By increasing the stamping speed, the heat loss becomes lower, the corresponding temperature is higher when the plate breaks, the strain hardening index is smaller, and the uniform deformation ability of the plate under load is weak. Therefore, the maximum downforce displacement of the plate decreases gradually with the increase in the stamping speed. In the forming process, the forming speed should be as small as possible. When the material meets the forming performance, the speed can be appropriately increased in order to save time and cost.
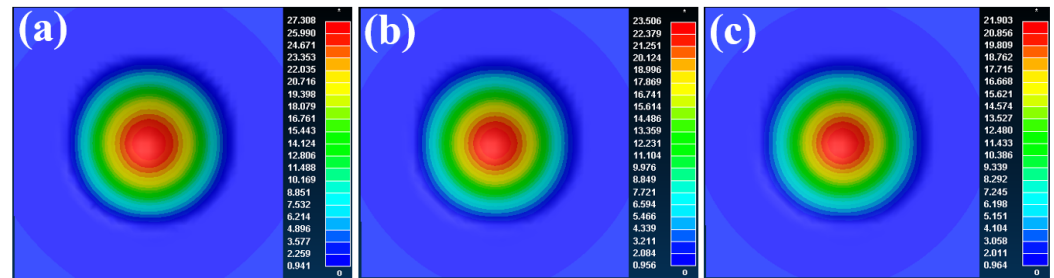
Figure 8. Nephogram of displacement corresponding to 22MnB5 steel under different forming speeds: (**a**) 2.5 mm/s; (**b**) 25 mm/s; (**c**) 250 mm/s.

Figure 9 is the nephogram of thinning rate corresponding to critical fracture time at different forming speeds. The maximum thinning rates corresponding to the critical breaking time at different forming speeds are 28.615%, 25.598%, and 19.992%, respectively. With the increase in forming speed, the pressing displacement corresponding to the critical breaking time of 22MnB5 steel gradually decreases, the load that can be borne in the thickness direction of 22MnB5 steel decreases, and the corresponding thinning rate decreases. Under the same thickness, the faster the forming speed, the easier the workpiece is to crack, and the greater the material thinning rate. Under the same specification, the workpiece obtained is light in weight.
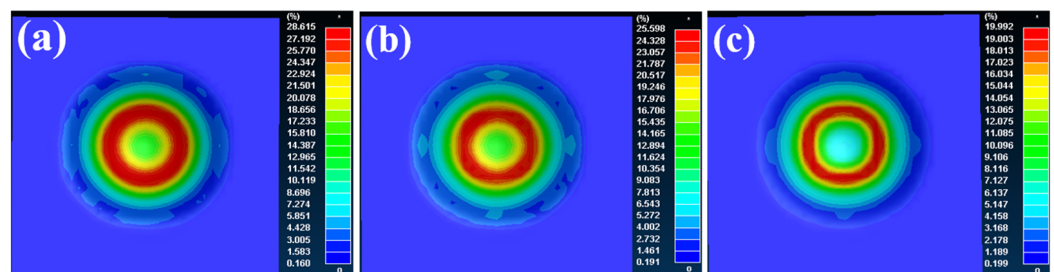
Figure 9. Nephogram of thinning rate corresponding to 22MnB5 steel under different forming speeds: (**a**) 2.5 mm/s; (**b**) 25 mm/s; (**c**) 250 mm/s.

Figure 10 is the cloud diagram of the temperature field corresponding to the critical fracture time of different initial deformation temperatures. It can be observed that when the initial forming temperature of the 22MnB5 steel is higher, the higher the temperature corresponding to the critical fracture time. However, due to the heat transfer and heat conduction between the 22MnB5 steel and the die and the cooling system, the temperature field corresponding to the 22MnB5 steel at the critical fracture time is not different. The temperature in the center of the contact part between the 22MnB5 steel and the punch is the highest, and the further away from the center, the lower the temperature. The temperature distribution near the center is uneven.

Figure 11 is the nephogram of displacement corresponding to the critical fracture time of the 22MnB5 steel under different initial deformation temperatures. It could be found that the maximum downforce displacement of the plate with different initial deformation temperatures at the critical fracture time was 27.219 mm, 29.037 mm, 25.422 mm or 24.822 mm,

respectively. The maximum downforce displacement increased with the increase in the initial deformation temperature, reached the maximum at 700 °C, and then decreased with the increase in the initial deformation temperature.
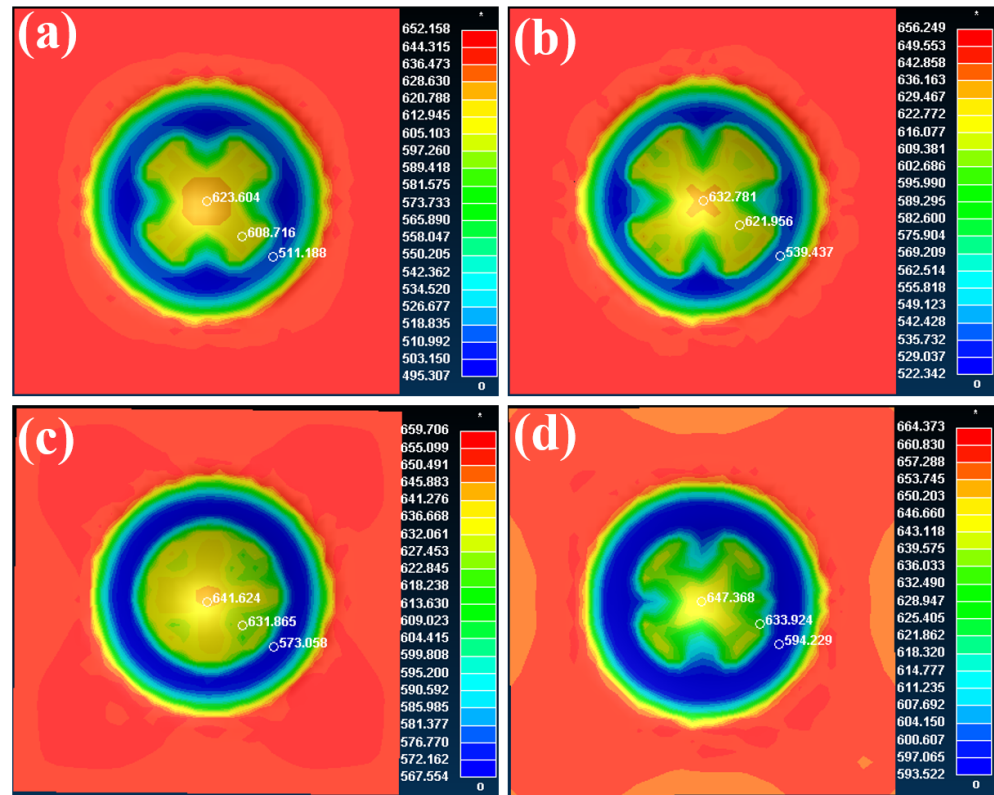
Figure 10. Nephogram of the temperature field corresponding to 22MnB5 steel under different initial deformation temperatures: (**a**) 600 °C; (**b**) 700 °C; (**c**) 800 °C; (**d**) 900 °C.
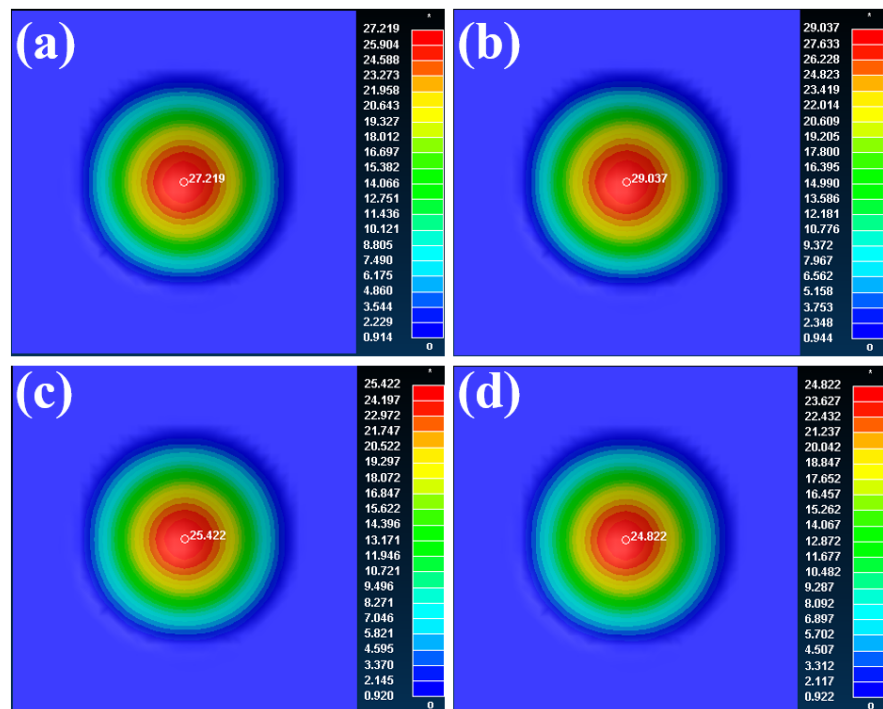
Figure 11. Nephogram of displacement of 22MnB5 steel at different initial forming temperatures: (**a**) 600 °C; (**b**) 700 °C; (**c**) 800 °C; (**d**) 900 °C.

Figure 12 is the cloud chart of the thinning rate corresponding to the critical fracture time at different initial deformation temperatures. It can be seen that the maximum thinning rate corresponding to different initial forming temperatures at the critical fracture time was 27.061%, 31.240%, 28.231% and 24.752%, respectively, which was the same as the law of downforce displacement. It increased with the increase in the initial deformation temperature of the plate. The greater the downforce displacement, the greater the thinning rate. The thinning rate reached the maximum at 700 °C. Thereafter, the thinning rate decreased with the increase in the initial deformation temperature of the plate. The area with the largest thinning rate was located around the contact center between the punch and the plate. Combined with the analysis of the temperature field nephogram, it was found that the area with the most serious thinning was located in the area with uneven temperature distribution.
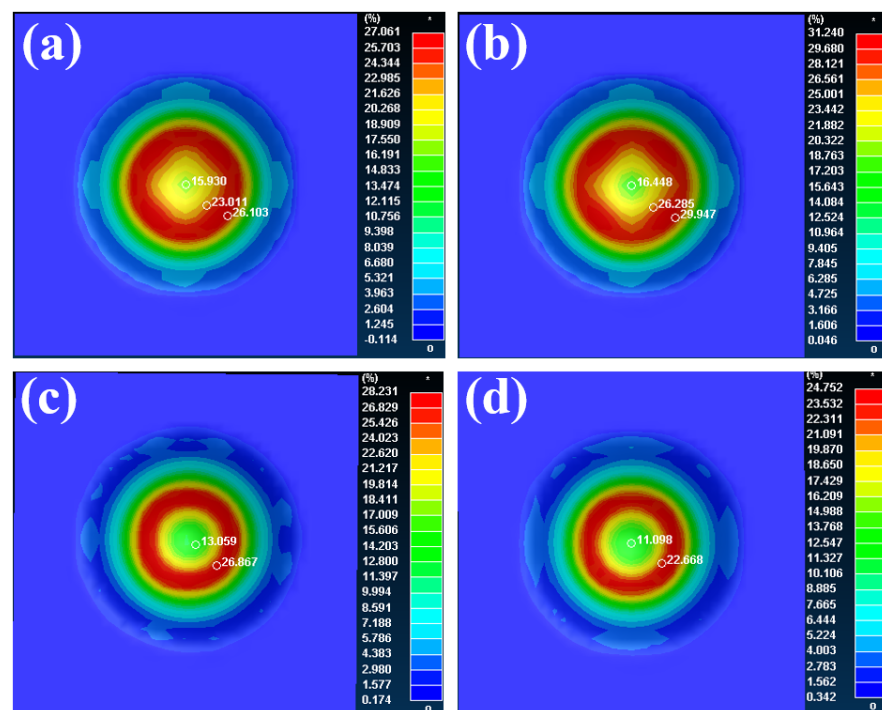
Figure 12. Nephogram of thinning rate of 22MnB5 steel under different initial deformation temperatures: (**a**) 600 °C; (**b**) 700 °C; (**c**) 800 °C; (**d**) 900 °C.

3.3. Establishment of Hot-Forming Limit Diagram for 22MnB5 Steel

To study the forming limit of 22MnB5 steel, we set the forming temperature to 700 °C, and the forming speed was set to 25 mm/s to perform the cup bulging simulation on the 22MnB5 steel plate. To analyze the post-processing results and identify the critical instability moments for different plate widths, the criterion combining the maximum punch force with the strain path transition was utilized, and the critical instability moments for different plate widths were identified. Figures 13 and 14 show the axial and radial strain nephograms, respectively, at the critical rupture moments for plate widths of 20 mm and 180 mm.

The analysis and extraction of the axial and radial strain points under different strain paths are depicted in Figures 13 and 14, and their values are shown in Table 3. The hot-forming limit diagram of the 22MnB5 steel plate can be obtained by fitting (as shown in Figure 15). It can be found that the primary and secondary strains on the left side of the FLD curve are linear when the secondary strain is less than 0. For the part where the secondary strain is greater than 0, the right side of the FLD curve shows a parabolic shape by quadratic fitting.
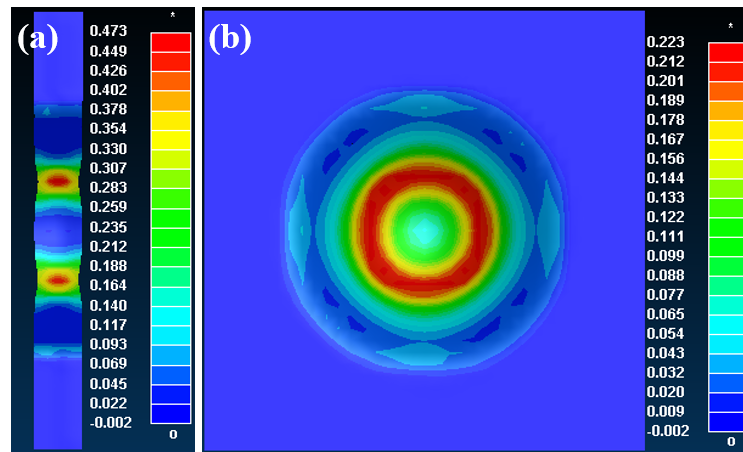
Figure 13. Nephogram of axial strain of critical fracture when plate widths are 20 mm and 180 mm. (**a**) 20 mm, (**b**) 180 mm.
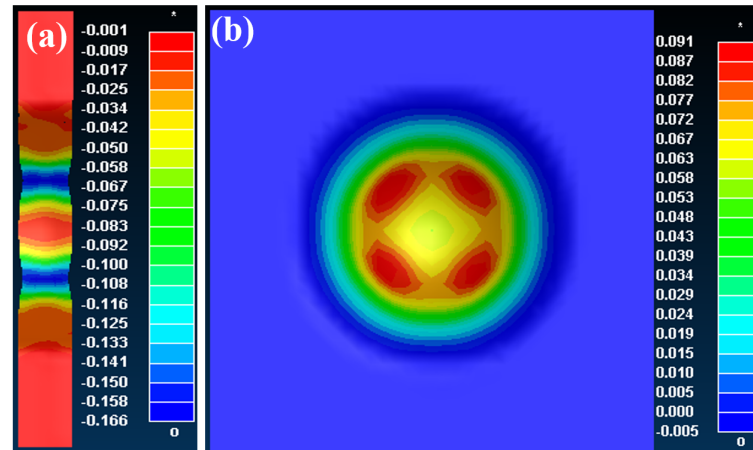
Figure 14. Nephogram of radial strain of critical fracture when plate widths are 20 mm and 180 mm. (**a**) 20 mm, (**b**)180 mm.

Table 3. Axial strain and radial strain points under different strain paths.

Radial strain	−0.169	−0.172	−0.186	−0.146	−0.009	−0.05	0.002	0.048	0.103	0.131	0.153
Axial strain	0.441	0.46	0.456	0.422	0.337	0.347	0.311	0.332	0.349	0.366	0.387
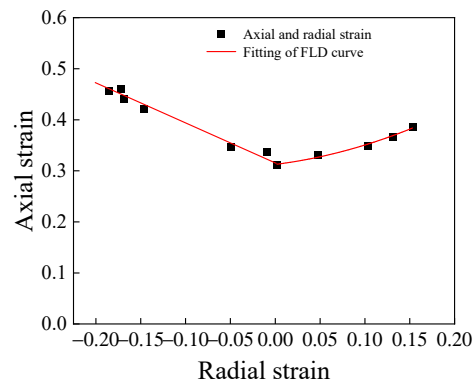
Figure 15. The hot-forming limit diagram of the 22MnB5 high strength steel plate at 700 °C.

3.4. Hot-Stamping Experiment of the 22MnB5 High-Strength Steel Plate

The 22MnB5 high strength steel with the same specifications as the simulation was selected for the hot stamping bulging experiment. Based on the simulation analysis results,

the hot stamping forming temperature of 700 °C and the pressing speed of 2.5 mm/s were selected to carry out the hot stamping bulging experiment. In order to keep the temperature field relatively uniform during forming, the hot stamping expansion experiment flow was as follows: (1) Heat the stamping die to 650 °C; (2) heat the 22MnB5 high strength steel plate to 930 °C using a resistance furnace and maintain at this temperature for 10 min. The plate is then transferred into the stamping die, to wait for the hot stamping experiment when the plate was cooled to 700 °C; (3) obtain force and displacement data from the data collector. Figure 16 shows the force–displacement curve during stamping when the plate width is 20 mm. Through curve analysis, record the corresponding pressing depth value and maximum punch force for plates with different widths after stamping, as shown in Table 4. It can be found that in addition to the 20 mm wide plate, the stamping depth value is relatively similar. The maximum punch force increases with the increase in plate width.
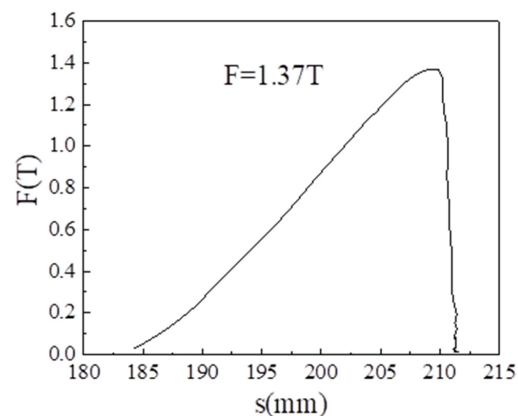
Figure 16. Force–displacement curve during stamping for the plate of 20 mm width.

Table 4. Pressing depth and maximum punch force after stamping with different plate widths.

Plate width (mm)	20	40	60	80	100	120	140	160	180
Stamping displacement (mm)	34.0	25.9	27.6	26.7	27.1	25.2	26.3	27.4	27.6
Maximum punch force (T)	1.37	1.98	2.42	3.25	3.83	4.28	5.62	5.78	6.54

The hot stamping experiment was repeated twice, each with a width of 20–180 mm at 700 °C. Figure 17 shows the maximum principal strain diagram of the hot-stamping-forming simulation and experiment with 22MnB5 steel plate widths of 60 mm and 180 mm, respectively. It could be found that under the same stamping displacement, for the corresponding area to the maximum principal strain, the simulation results were almost the same as the 22MnB5 steel fracture area after the experiment; Table 5 shows the punch force corresponding to the experimental and simulation results under the same stamping displacement. It can be seen that the results of numerical modelling were very close to the experimental results, indicating that the results obtained by the simulation method were reliable.
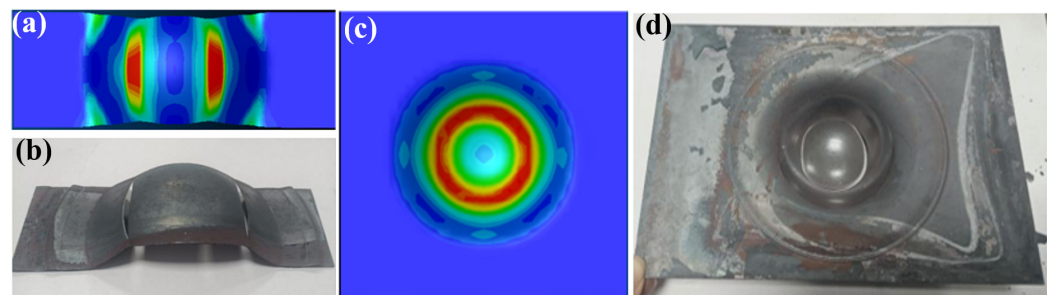
Figure 17. Comparison chart of the maximum principal strain nephogram and plate state after experiments with different plate widths: (**a**) 60 mm; (**b**) 60 mm; (**c**) 180 mm; (**d**) 180 mm.

Table 5. Punch force of the experimental and simulation results under the same downforce displacement.

Plate width (mm)	20	40	60	80	100	120	140	160	180
Stamping displacement (mm)	30	23	25	25	25	23	24	25	25
Punch force of experiment (T)	0.91	1.8	2.4	3.2	3.8	4.2	5.6	5.6	6.5
Punch force of simulation (T)	0.88	1.5	2.6	3.0	3.75	4.0	5.8	5.5	6.3

4. Conclusions

The applicability of the instability criterion was analyzed by simulating different sheet widths of 22MnB5 steel. The influence of forming speed and initial deformation temperature on the formability of the 22MnB5 steel plate was studied, and the forming limit diagram of 22MnB5 steel at 700 °C was investigated. The following conclusions can be drawn:

1. In the numerical simulation of bulging experiments, the maximum punch force criterion was applicable to a plate width of 20~80 mm, and the maximum strain path transition criterion was applicable to 100~180 mm.
2. The formability of 22MnB5 steel decreases with the increase in deformation speed and increases with the rise in initial deformation temperature of 22MnB5 steel, reaching the maximum when the initial temperature of 22MnB5 steel is 700 °C.
3. The limit strain point is determined by the instability criterion, and the hot-forming limit diagram of the 22MnB5 HF steel plate at 700 °C and 25 mm/s is obtained by fitting. It is found that the axial strain and radial strains are linear when the radial strain is less than 0, and the parts where the radial strain is greater than 0 can be fitted by binomial. Through experimental verification, it is found that the simulation results obtained by DYNAFORM finite element simulation software are reliable.

Author Contributions: Conceptualization, W.H.; Methodology, B.Y.; Software, X.Z. and M.L.; Formal analysis, S.S. and Q.M.; Writing—review & editing, B.W. All authors have read and agreed to the published version of the manuscript.

Data Availability Statement: The original contributions presented in the study are included in the article, and further inquiries can be directed to the corresponding author.

Conflicts of Interest: Min Li was employed by the Weichai Power Co., Ltd. The remaining authors declare that the research was conducted in the absence of any commercial or financial relationships that could be construed as a potential conflict of interest.

References

1. Bao, L.; Liu, W.J.; Wang, B.; Li, H.P.; You, X.P.; Zhou, Q.; Liu, M.; Gao, S.R. Experimental investigation on partition controllable induction heating-hot stamping process of high-strength boron alloyed steel plates with designable temperature patterns. *J. Mater. Res. Technol.* **2020**, *9*, 13963–13976. [CrossRef]
2. Guo, J.; Liu, H.L.; Li, X.D.; Yang, T.Y. Fracture behavior of the hot-stamped PHS2000 steel based on GISSMO failure model. *Metals* **2023**, *13*, 1360. [CrossRef]
3. Liang, L.Z.; Hui, L.J.; Sheng, S.Y.; Ze, Y.C. automobile manufacturing. *J. Mech. Sci. Technol.* **2009**, *23*, 1924–1931. [CrossRef]
4. Hu, Y.J.; Wang, Z.L.; Wang, Y.Q. Selection of distributed manufacturing environments based on genetic algorithm for automobile gears. *Mater. Manuf. Process.* **2013**, *28*, 1268–1275. [CrossRef]
5. Quan, G.Z.; Zhan, Z.Y.; Zhang, L.; Wu, D.S.; Luo, G.C.; Xia, Y.F. A study on the multi-phase transformation kinetics of ultra-high strength steel and application in thermal-mechanical-phase coupling simulation of hot stamping process. *Mat. Sci. Eng. A* **2016**, *673*, 24–38. [CrossRef]
6. Sun, H.; Yao, S.J.; Tang, Q.H.; Rong, R.L.; Chu, G.N.; Auer, P.; Domitner, J. Short-wave infrared heating of 22MnB5 steel with adjusted surface emissivity for press hardening of tailored-strength components. *J. Manuf. Process.* **2024**, *120*, 74–85. [CrossRef]
7. Simonetto, E.; Ghiotti, A.; Bruschi, S. Numerical modelling of direct hot tube rotary draw bending of 22MnB5 high strength steel. *CIRP J. Manuf. Sci. Technol.* **2022**, *37*, 547–558. [CrossRef]

8. Li, T.T.; Xie, X.L.; Xu, J.F.; Li, R.F.; Qi, K.; Zhang, X.Q.; Yue, H.Y.; Zhao, Y.; Qiao, L. Research on AZ31 Mg alloy/22MnB5 steel pinless friction stir spot welding process and interfacial temperature field simulation. *J. Mater. Res. Technol.* **2023**, *26*, 3710–3725. [CrossRef]

9. Yao, S.J.; Feng, L.; Yang, D.L.; Han, D.X.; Liu, Y.; Li, Q.; Chao, B.J. A potential hot stamping process for microstructure optimization of 22MnB5 steels characterized by asymmetric pre-rolling and one-or two-step pre-heating. *J. Mater. Process. Technol.* **2018**, *254*, 100–107. [CrossRef]

10. Chen, W.J.; Song, H.W.; Lazarescu, L.; Xu, Y.; Banabic, D. Formability analysis of hot-rolled dual-phase steel during the multistage stamping process of wheel disc. *Int. J. Adv. Manuf. Technol.* **2020**, *110*, 1563–1573. [CrossRef]

11. Huang, D.; Kodur, V.; Wang, W.Y. Temperature-dependent properties of high-strength steel for evaluating the fire resistance of structures. *Adv. Struct. Eng.* **2023**, *26*, 2265–2281. [CrossRef]

12. Hart-Rawug, T.; Buhl, J.; Horn, A.; Bambach, M.; Merklein, M. A unified model for isothermal and non-isothermal phase transformation in hot stamping of 22MnB5 steel. *J. Mater. Process. Technol.* **2023**, *313*, 117856. [CrossRef]

13. Singh, A.; Bhattacharya, A.; Butcher, C. Experimental artefacts affecting characterization of the evolving interfacial heat transfer coefficient in hot stamping of Al-Si coated 22MnB5 steel. *Appl. Thermal. Eng.* **2024**, *24*, 121604. [CrossRef]

14. Liu, H.P.; Lu, X.W.; Jin, X.J.; Dong, H.; Shi, J. Enhanced mechanical properties of a hot stamped advanced high-strength steel treated by quenching and partitioning process. *Scr. Mater.* **2011**, *64*, 749–752. [CrossRef]

15. Couto, C.P.; Revilla, R.I.; Politano, R. Influence of austenitisation temperatures during hot stamping on the local electrochemical behaviour of 22MnB5 steel coated with hot-dip Al-Si. *Corros. Sci.* **2021**, *190*, 109673. [CrossRef]

16. Lkeda, Y.; Ni, H.C.; Chakraborty, A. Segregation-induced grain-boundary precipitation during early stages of liquid-metal em brittlement of an advanced high-strength steel. *Acta Mater.* **2023**, *259*, 1359–6454.

17. Naderi, M.; Uthaisangsuk, V.; Prahl, U. A Numerical and experimental investigation into hot stamping of boron alloyed heat-treated steels. *Steel Res. Int.* **2009**, *79*, 77–84. [CrossRef]

18. Dabuel, A.; Fabio, M. Phase transformation temperatures and Fe enrichment of a 22MnB5 Zn-Fe coated steel under hot stamping conditions. *J. Mater. Res. Technol.* **2019**, *9*, 629–635.

19. Venturato, G.; Ghiotti, A.; Bruschi, S. Stress-state dependent formability modelling in hot stamping. *Prod. Eng.* **2020**, *14*, 105–114. [CrossRef]

20. Zhuang, W.; Wang, P.; Xie, D.; Shi, H. Experimental study and a damage model approach to determine the effect of hot forming deformation on the service performance of 22MnB5 steel. *J. Manuf. Process.* **2019**, *47*, 10–21. [CrossRef]

21. Chen, J.; Zheng, X.; Liu, Y. Theoretical prediction of high strength steel 22MnB5 forming limit in high temperature based on M-K model. *Procedia Eng.* **2017**, *207*, 632–639. [CrossRef]

22. Zhou, J. *Research on Thermal Simulation Experiment and Damage Evolution Modeling and Simulation of Boron Steel Hot Stamping*; Beijing University of Science and Technology: Beijing, China, 2015.

23. Guo, J.; Zhan, M.; Wang, X. Ductile fracture criterions for hot forming process of Ti-6Al-2Zr-1Mo-1V alloy sheet. *J. Cent. South Univ.* **2017**, *48*, 2294–2300.

24. Zhang, X.; Zeng, W.; Shu, Y.; Zhao, Y.; Yu, H.; Zhou, Y. Study on cracking criterion of Ti40 flame retardant alloy based on Zener Hollomon factor. *Rare Met. Mater. Eng.* **2008**, *4*, 604–608.

25. Neumann, R.; Schuster, S.; Gibmeier, J. Two-scale simulation of the hot stamping process based on a Hashin–Shtrikman type mean field model. *J. Mater. Process. Technol.* **2019**, *267*, 124–140. [CrossRef]